JVSTA Journal of Vacuum Science & Technology A

Atomic bonding effects in annular dark field scanning transmission electron microscopy. II. Experiments

Michael L. Odlyzko, Jacob T. Held, and K. Andre Mkhoyan

Citation: Journal of Vacuum Science & Technology A **34**, 041603 (2016); doi: 10.1116/1.4954877
View online: http://dx.doi.org/10.1116/1.4954877
View Table of Contents: http://scitation.aip.org/content/avs/journal/jvsta/34/4?ver=pdfcov
Published by the AVS: Science & Technology of Materials, Interfaces, and Processing

Atomic bonding effects in annular dark field scanning transmission electron microscopy. II. Experiments

Michael L. Odlyzko, Jacob T. Held, and K. Andre Mkhoyan[a)]
Department of Chemical Engineering and Materials Science, University of Minnesota, Minneapolis, Minnesota 55455

(Received 31 May 2016; accepted 9 June 2016; published 30 June 2016)

Quantitatively calibrated annular dark field scanning transmission electron microscopy (ADF-STEM) imaging experiments were compared to frozen phonon multislice simulations adapted to include chemical bonding effects. Having carefully matched simulation parameters to experimental conditions, a depth-dependent bonding effect was observed for high-angle ADF-STEM imaging of aluminum nitride. This result is explained by computational predictions, systematically examined in the preceding portion of this study, showing the propagation of the converged STEM beam to be highly sensitive to net interatomic charge transfer. Thus, although uncertainties in experimental conditions and simulation accuracy remain, the computationally predicted experimental bonding effect withstands the experimental testing reported here. © *2016 American Vacuum Society*.
[http://dx.doi.org/10.1116/1.4954877]

I. INTRODUCTION

Conventional implementations of transmission electron microscopy (TEM) image simulation, both multislice[1,2] and Bloch wave,[3] model the electrostatic potential of a solid as that of a collection of unbonded neutral atoms; this approximation is known as the independent atom model (IAM). The companion study[4] considered the sensitivity of annular dark field (ADF) scanning TEM (STEM) imaging to valence charge distribution by comparing IAM simulations against charge-transfer-inclusive simulations; extensive computational studies found that light-element single crystals with net interatomic charge transfer exhibited significant differences in ADF-STEM image contrast relative to IAM images. These depth-dependent differences were found to arise because polar bonding alters the channeling[5,6] and beam spreading[7–10] of focused STEM probes, which in turn alters the ADF-STEM imaging for any combination of incident probe, detector geometry, and material temperature; this applied even to the high-angle ADF (HAADF) imaging mode, where bonding effects on coherent scattering into the detector are minimized.

The significance of such computational predictions is intriguing in the context of the aberration corrected[11,12] STEM era, where sub-Angstrom resolution HAADF-STEM imaging,[13,14] electron energy-loss spectroscopy (EELS),[15,16] and x-ray energy-dispersive spectroscopy (XEDS)[17,18] are routinely performed and found to qualitatively agree with IAM simulations.[9,10,19] Furthermore, an extensive literature showing convincing quantitative agreement between IAM simulation and quantitatively calibrated experimental imaging has emerged: atomic resolution HAADF-STEM (Ref. 20) and bright-field-STEM (Ref. 21) imaging of $SrTiO_3$, compositional HAADF-STEM imaging of III–V alloys,[22] atomic resolution imaging of heavy-element ceramics $PbWO_4$ (Ref. 23) and LaB_6,[24] atomic-resolution HAADF-STEM and EELS imaging of $DyScO_3$,[25] atomic resolution thickness measurement of AlN,[26] and three-dimensional dopant location in $SrTiO_3$ (Ref. 27) and AlN,[28] to name some prominent examples. All of the preceding studies involve systems with highly polar bonding and found good agreement between experimental ADF-STEM images and IAM frozen-phonon multislice simulations.

Of these systems, only AlN has been examined systematically in the companion study, predicting a subtle but measureable effect of bonding on image contrast. Because chemical bonding essentially alters the symmetry of the valence charge distribution of a solid, and in special cases of polar bonding also alters the net charge on each atom, it may have vanishing significance for the ADF-STEM imaging of most crystals: where there is little or no fractional change in the electronic charge on an atom, there should be minimal or no effect on the scattering of fast electrons from those screened atomic nuclei. This may account for the robust adequacy of IAM simulation in most materials systems, but this hypothesis is presently set aside for future testing.

In this study, attentions are rather focused on a system that seems most promising for exhibiting experimentally measureable bonding-sensitivity, namely, a light-element crystal with highly polar bonding that has already been analyzed in the companion study. By attempting a complete characterization of quantitative HAADF-STEM imaging of AlN, experimental images can be compared very precisely to simulations employing various bonding models to examine possible bonding effects. Insofar as significant bonding effects can be ascertained, this may encourage the application of bonding-inclusive simulation not only in analyzing ADF-STEM imaging of perfect single crystals, but also in characterizing important defect systems in polar materials, such as ordered point defects,[29] dislocations, and epitaxial interfaces.[30]

II. METHODS

Single crystal AlN, a material found to exhibit strong bonding effects in the companion study, was deemed to be

[a)]Author to whom correspondence should be addressed; electronic mail: mkhoyan@umn.edu

the most suitable material for experimental study. AlN can be grown as a high-quality single crystal and is thus employed as a substrate for epitaxial thin film growth of other III–V materials. It has a wurtzite crystal structure and a bond length of 0.19 nm. With a band gap of 6.0 eV, a Pauling $\Delta X = 1.43$, and a formal net charge of ± 3, AlN is an insulator with large net interatomic charge transfer.

Observation of bonding-dependent image contrast requires imaging these crystals at zone axes where the columns are spaced sufficiently far apart to be resolved by an aberration-corrected electron probe, with each column being composed entirely of one type of atom (e.g., Al in separate columns from N). These conditions are satisfied by the $\langle \bar{2}110 \rangle$ orientation of AlN, corresponding to an intercolumn spacing of 0.11 nm (Fig. 1).

AlN was prepared for STEM imaging by mechanical wedge polishing of a (0001) wafer grown by physical vapor transport, provided by Nitride Crystals, Inc. Subsequent treatments included etching in a dilute HF acid solution to remove the surface damage layer, deposition of a colloidal silver coating at the back to produce better conductive contact to the washer, and Ar/O_2 plasma cleaning to remove hydrocarbon contaminants.

STEM imaging was performed using an aberration-corrected FEI Titan G2 60–300 equipped with a CEOS DCOR probe corrector, high-brightness XFEG Schottky field emission gun, Fischione 2100 HAADF detector, Gatan BM-Ultrascan CCD camera, and Gatan Enfinium ER parallel EELS spectrometer. The microscope was operated at 200 keV in low-dose-rate (a 10.0 pA beam current as measured from calibrated fluorescent screen intensity, with dwell times of 2–12 μs per pixel) conditions and a large convergence semiangle of 30 mrad, conditions producing extremely high spatial resolution (up to 15 nm^{-1} information transfer) while maintaining acceptable levels of image noise, specimen drift, and negligible charging. Projection lens settings used for very thin specimens of AlN corresponded to a 55 mrad HAADF inner semiangle and 11 mrad EELS semiaperture, while those used in all other conditions corresponded to a 68 mrad HAADF inner semiangle and 13 mrad EELS semiaperture. Effective HAADF outer angle was not determined experimentally, but taken as 200 mrad, as estimated by FEI and used to good quantitative agreement in another study.[24]

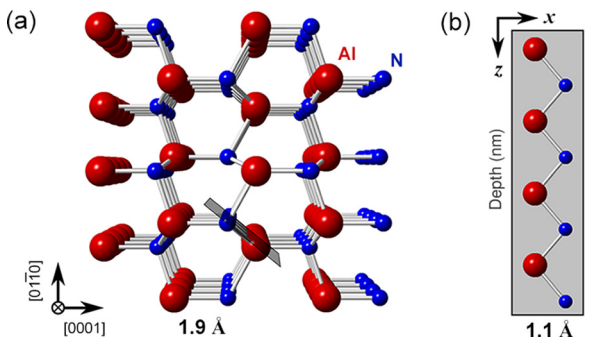

FIG. 1. (Color online) (a) Perspective crystal structure rendering of $\langle \bar{2}110 \rangle$-oriented AlN. (b) The structure of the crystal with nearest-neighbor columns along the depth. Both nearest-neighbor and second-nearest-neighbor intercolumn spacings are indicated. The nearest-neighboring column is just over half of a bond length away, causing significant coupling of the STEM beam intensity between oppositely charged columns.

All raw images were processed by taking regions of uniform contrast, first applying a moderate low-pass filter (8 nm^{-1} passband with Butterworth smoothing of cutoff), and cross-correlating 20–100 images together to form a reference image with high signal-to-noise ratio (SNR). Subsequently, the same images were low-pass-filtered to higher resolution (16 nm^{-1} passband with Butterworth smoothing of cutoff) and cross-correlated to form a many-unit-cell cross-correlated image with full information transfer and high SNR. Edge artifacts, attributable to pervasive image distortions (uneven rastering and specimen drift) and the cutting of images into patches not exactly commensurate with the crystal unit cell, were cropped away to leave integer multiples of unit cells. The remaining sections of such images could then be reliably spline-interpolated for matching image simulation (by means of image rotation and matching of experiment image sampling to the simulation sampling), allowing straightforward comparison between simulated and experimental images. Crystallographically identical linescans from within the final interpolated experimental image were averaged to produce representative experimental linescans.

Imaging was performed with a detector dynamic range spanning approximately 0–2.5 pA (0–0.25P_0 in terms of incident probe current P_0) in the most sensitive sections of the detector. Owing to the sensitivity of imaging to detector nonuniformity,[31] detector mapping was done in each session using the same settings of detector gain ("contrast") and voltage offset ("brightness") as used for HAADF imaging, with an incident beam current of 1.5 pA (0.15P_0). The method employed to convert raw images into quantitatively calibrated images, described below, adapts the notation and terminology of a recently published study that employed an equivalent method.[32]

Detector maps were converted into reciprocal space measurements of detector response $D(\vec{k})$ ($\vec{k}$ is a reciprocal-space vector, for small angles $\theta \approx \lambda k$), such that the dark-level subtracted detector signal $I(\vec{k})$ was related to any normalized detector mapping current $N_M \equiv P_M/P_0$ (P_M is the probe current used when mapping the detector) according to $I(\vec{k}) = N_M D(\vec{k})$. The average detector response $\bar{D}$ (over a large, highly uniform region of the detector) was calculated as

$$\bar{D} = \frac{\int D(\vec{k}) d^2\vec{k}}{\int d^2\vec{k}}. \quad (1)$$

Combining the measured nonuniform detector response $D(\vec{k})$ (universal for a given detector setting) with a knowledge of the scattered flux distribution $F(\vec{r}, \vec{k})$ (specific to incident probe parameters, incident probe position, projection optics settings, specimen structure, specimen thickness), the normalized imaging current $N(\vec{r})$ and detector signal $I(\vec{r})$

are each varying as a function of probe position $\vec{r}$ to form the ADF STEM image as follows (both integrations are performed over the illuminated section of the detector):

$$N(\vec{r}) = \int F(\vec{r},\vec{k})d^2\vec{k}, \tag{2}$$

$$I(\vec{r}) = \int D(\vec{k})\,F(\vec{r},\vec{k})d^2\vec{k}. \tag{3}$$

A damping coefficient $\xi(\vec{r})$ can then be defined to capture the attenuation of experimentally detected intensity relative to signal measured by a perfect detector, where $D(\vec{k}) = \bar{D}$ for all $\vec{k}$, which varies with probe position $\vec{r}$

$$I(\vec{r}) = \bar{D}\xi(\vec{r})N(\vec{r}). \tag{4}$$

However, because it is essentially the magnitude rather than the reciprocal-space shape of the scattered flux distribution that is position-dependent, a single position-independent damping factor, ξ_0, and the detected signal intensity can be simply transformed to a scale of normalized imaging current, described as

$$N(\vec{r}) = \frac{I(\vec{r})}{\bar{D}\,\xi_0}. \tag{5}$$

This quantification process is illustrated in Fig. 2.

The study by Martinez *et al.*[32] that set forth our method of STEM quantification also carefully compared results obtained using this method to the standard quantification routines (those applying nonuniform detector response to simulation rather than inverting the response from experimental data), and found them to be equivalent. Because experimentally recorded flux distribution, $F(\vec{r},\vec{k})$, measurements using the CCD at the back focal plane were within the noise level at high scattering angles, the scattered flux distribution was estimated from position-averaged convergent beam electron diffraction (Ref. 33) (PACBED) simulations performed for the estimated thickness. Thickness information was available from a combination of experimentally recorded data: low-loss EELS spectra, PACBED patterns, and "position-averaged HAADF"[26] (PAHAADF) imaging. Because the damping factor ξ_0 changes very gradually as a function of increasing thickness, PAHAADF alone was sufficient to estimate thickness to ± 1 nm, and was corroborated by low-loss EELS and PACBED data for all of the thicknesses reported here. Crystal orientation was determined using PACBED data.

Even with convergence angle, detector geometry, crystal orientation, and crystal thickness determined from experimental data, some probe parameters remain undetermined: defocus, coherent low-order aberration effects (especially twofold astigmatism), and the effective demagnified source distribution. Without having acquired focal series data to assist in the determination of defocus, low-order aberrations, and source distribution, an iterative procedure was used to estimate experimental imaging parameters. The orientation of twofold astigmatism was estimated from visible asymmetry in the high-SNR images. Simulated images with different magnitudes of twofold astigmatism in this orientation were then checked in slight underfocus and slight overfocus conditions to produce a range of possible defocus/astigmatism combinations. Finally, different source distributions were considered, under the constraint that convolution of those

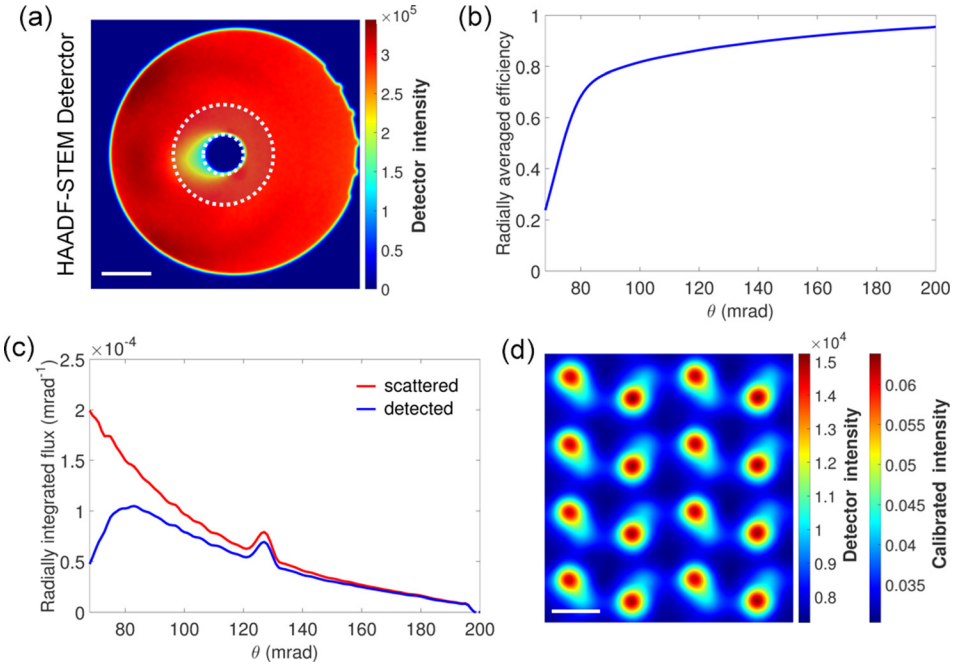

FIG. 2. (Color online) Quantification of an experimental HAADF image. (a) HAADF detector response map $D(\vec{k})$ acquired with 1.5 pA incident current; 68–200 mrad conditions correspond to a scale bar of length 200 mrad (800 nm^{-1}) and an active region indicated by the transparent mask. (b) Radially averaged efficiency profile for 68–200 mrad collection. (c) Radially integrated fluxes for 68–200 mrad collection, where the scattered flux is attenuated by the efficiency profile to determine the detected flux. (d) Cross-correlated image of 80 nm thick AlN using a 68–200 mrad detector, both in terms of detected intensity $I(\vec{r})$ and quantitative calibrated intensity $N(\vec{r})$ ($\bar{D} = 3.10 \times 10^5$, $\xi_0 = 0.77$). The scale bar is 2 Å.

source distributions with simulated images simultaneously yielded a good fit to three different experimental measures: the width of atomic column features, the peak intensity of atomic columns in the image, and the "background" level of the image. Considering that there was no measureable change in gun emission current during time over which these experiments were performed, a single source distribution was applied to all simulations before they were compared to experimental data.

To include the effects of bonding using computational methods, three different bonding models were used: the IAM, the bonded crystal model (BCM), and the fully ionized model (FIM). In IAM, the charge density of the solid was calculated as the superposition of the charge densities of independent neutral atoms. In BCM, the charge density of the solid was calculated as the superposition of atomic ion-core charge densities with valence charge densities calculated by density functional theory (DFT). In FIM, the charge density of the solid was calculated as the superposition of the charge densities of independent full-valence-shell ions. The method for calculating the charge densities and transforming them into inputs for multislice simulation is detailed within the companion study.

Multislice simulations of each bonding model employed probe and transmission functions calculated on a 1024×1024 pixel grid, with a supercell of size $4.31 \times 3.98\,\mathrm{nm}^2$. The supercell corresponded to 8×8 tiling of the effective rectangular unit cell [$0.539 \times 0.498\,\mathrm{nm}^2$ for $\langle \bar{2}110 \rangle$-oriented AlN], allowing exact sampling of Bragg reflections. Probe positions were sampled on a 64×64 pixel grid within the rectangular unit cell of each crystal. Slice thicknesses were chosen to be the interplanar spacing along the beam direction for $\langle \bar{2}110 \rangle$-oriented AlN (0.155 nm), allowing the correct reproduction of higher-order Laue zone diffraction. To ensure accurate TDS-inclusive simulations, RMS thermal vibration values were determined from the experimental diffraction literature for AlN (Ref. 34) (3D RMS displacements of 10.7 and 11.6 pm for Al and N, respectively), and up to 20 frozen phonon configurations were sampled to form a given image or PACBED pattern. As is standard practice, neither the anisotropy of thermal vibrations nor the contributions of inelastic scattering were included in these simulations. Effects of finite source distribution were included by convolution of the source function with the simulated point-source images.

III. RESULTS AND DISCUSSION

Although it is BCM that emulates the bonding of real solids, it is instructive to compare BCM multislice simulations to the hypothetical extremes of nonexistent (IAM) and complete (FIM) charge transfer. If, within experimental uncertainty, BCM image simulations can be found to be a statistically significant better fit relative to IAM simulation, the effect of bonding on HAADF-STEM image contrast is experimentally demonstrated.

A. Experimental data

Cross-correlated images were obtained from regions of varying thickness on the AlN wedge specimen. Three thicknesses were chosen for focused quantitative analysis: $18 \pm$ nm (thickness 1), $50 \pm$ nm (thickness 2), and $80 \pm$ nm (thickness 3). As explained in the simulation section, this included both thicknesses with a predicted strong bonding effect (thicknesses 2 and 3) and that with a predicted negligible bonding effect (thickness 1). This was done because best-fitting simulations should match well for "control thicknesses" where the effect of bonding is predicted to be weak as well as thicknesses where it is predicted to be strong.

PACBED patterns and quantitatively calibrated HAADF-STEM images from these thicknesses are displayed in Fig. 3. Owing to the complex herring-bone contrast of the AlN in this orientation, imaging was performed with subtle twofold

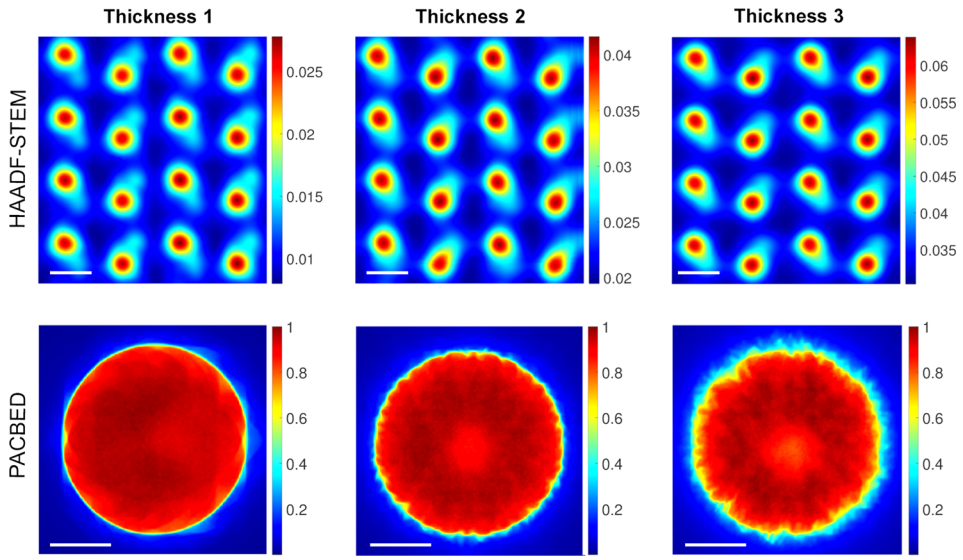

FIG. 3. (Color online) Quantitatively calibrated HAADF-STEM imaging of different sections of a $\langle \bar{2}110 \rangle$-oriented AlN sample. Thickness was determined by PAHAADF, and the orientation was determined by PACBED. For images, the HAADF intensities are quantitatively calibrated, and scale bar length is 2 Å. PACBED patterns are normalized relative to the most intense region of the pattern, and scale bar corresponds to 20 mrad ($8\,\mathrm{nm}^{-1}$).

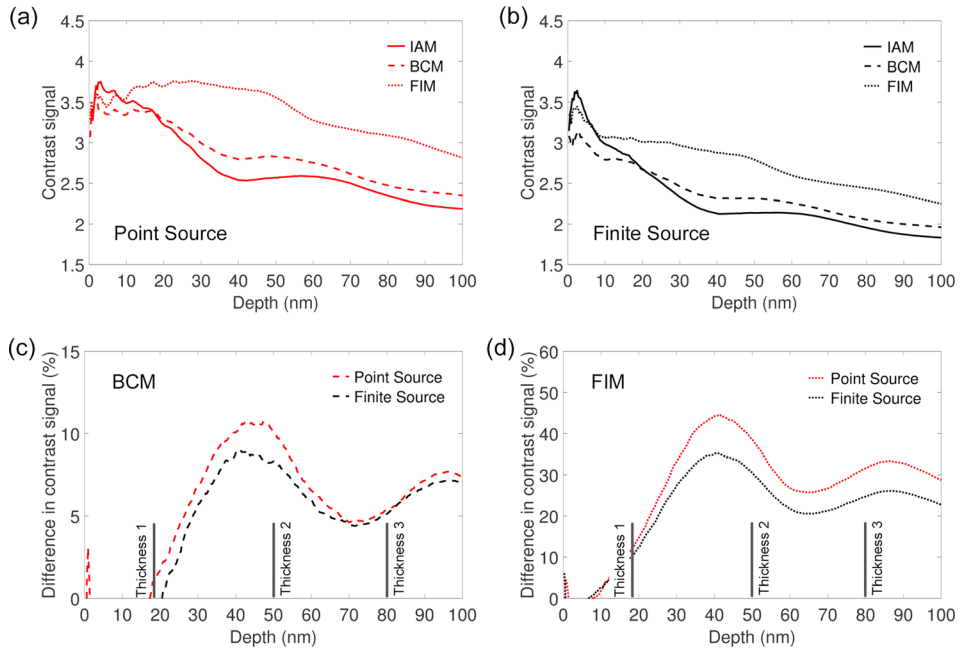

FIG. 4. (Color online) HAADF-STEM image contrast for AlN in both point-source and finite-source conditions. (a) and (b) Variation in contrast signal as a function of depth. (c) and (d) Differences in contrast signal relative to IAM.

astigmatism in the probe that was revealed only after cross-correlation.

Owing to very slight inhomogeneity of the images—due to some residual hydrocarbon contamination, surface damage, thickness variation—cross-correlated images also exhibit inhomogeneity. Representative linescans of these images can be constructed by averaging together linescans through each set of equivalent features in the experimental image.

B. Simulation of experiment

Bonding-inclusive multislice simulations of the companion study indicated a strong depth-dependence of the effect of bonding on image contrast. Employing an idealized probe for the HAADF-STEM imaging of these crystals—Gaussian focus, no low-order aberrations—the effect of bonding on multislice image simulations is summarized in Fig. 4, approximating a Gaussian of FWHM 0.5 Å as the source distribution for the finite source simulations. Strongest bonding effects in AlN are predicted to emerge at thicknesses 30 nm and above; while image contrast is most altered relative to IAM for FIM simulations, meaningful differences also exist between IAM and BCM. As discussed in the companion study, the effect of bonding on image contrast is robust relative to the blurring effect of a fine source distribution.

The set of experimental images examined include both thicknesses with a strong theoretically predicted bonding effect and those with a negligible effect (i.e., very small difference between IAM and BCM simulation predictions). With high-quality calibrated experimental data in hand, a direct comparison can be made between experiment and simulation. However, a meaningful comparison requires simulations to replicate as fully as possible the conditions of the experimental imaging.

Crystal thickness (neglecting small effects of surface reconstruction, damage, or contamination at the surfaces by treating the entire thickness as perfect) and crystal orientation were fixed based on experimental data. Although the mis-tilts of the experimental images were small, all being 6 mrad or lesser, the effect was included on account of computational studies[35,36] showing that even slight misorientation can measurably affect ADF-STEM image contrast of zone-axis-oriented single crystals. Fitting across all images yielded a good fit from a Gaussian-like function with longer-ranged tails, as determined in independent experimental characterizations[24,25,37] of high-brightness electron sources. In this study, the source distribution was modeled as a Gaussian of FWHM 0.5 Å, convolved with a Lorentzian of FWHM 0.1 Å. The effect of this source distribution is illustrated in Fig. 5 for an approximately aberration-free probe of the same beam energy and convergence angle as used in experiments.

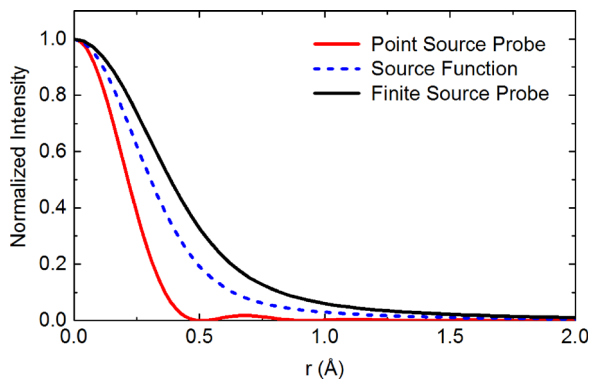

FIG. 5. (Color online) Radial profiles of the point-source electron probe, the estimated source distribution, and the finite-source probe. Including source size broadens the incident probe from a FWHM of 0.4 Å to a FWHM of 0.8 Å.

TABLE I. Summary of parameters used to simulate conditions of each AlN imaging experiment. Zero corresponds to Gaussian focus, while positive values of defocus correspond to overfocus.

	Sample thickness		
	18 nm	50 nm	80 nm
Mistilt (mrad)	6.0	0.5	2.5
Defocus (nm)	−2.5	+2.0	+1.5
Twofold astigmatism (nm)	0.6	0.0	0.6

Having estimated the source distribution by fitting to well-focused images, the simulated probe for each image was estimated as fully aberration-corrected apart from twofold astigmatism; this approximation was supported by stable measurements of very small higher-order aberrations made using the probe corrector software just prior to AlN imaging. With the orientation of twofold astigmatism being estimated from visible asymmetries in the images, it is the combination of twofold astigmatism amplitude and defocus that remain as tunable parameters. These parameters were set so as to have simulated images closely match both the overall contrast and linescan anisotropy of the images. Final parameters for imaging simulations of AlN are summarized in Table I.

C. Direct comparison of experiments and simulations

The resulting simulations are presented in Fig. 6 alongside experimental data. 2×1 unit cell images are plotted side-by-side, and linescans between nearest-neighboring columns are analyzed for quantitative comparison. Experimental linescan data are plotted with an error bar at each point representing the standard deviation; because the SNR of the images after filtering and cross-correlation is extremely high, this uncertainty essentially reflects inhomogeneities in the image due to specimen drift, scan distortion, and intrinsinc fine-scale structural variation. Even with these uncertainties being accounted for, good overall agreement is found between carefully tuned frozen-phonon multislice simulations and quantitatively calibrated ADF-STEM imaging, in concert with other quantitative STEM studies of AlN.[26,28]

For all of the conditions examined above, overall contrast matches closely, but no simulation perfectly matches both pairs of linescans. This very slight mismatch highlights the difficulty of exactly reproducing the probe conditions in simulation. However, a quantitative analysis of sum-squared error shows that the BCM model is the better fitting model for the thicknesses where significant bonding-dependent differences exist (Fig. 7). Two different approaches were applied to align the theoretical linescans to experimental ones: (1) they are aligned by matching the unique peak positions corresponding to Al column and (2) they are aligned by minimizing the sum-squared error (minimizing the value of χ^2). The uncertainties in evaluating χ^2 were estimated using the results obtained from reference set for 18 nm thick sample.

These results do demonstrate varying levels of agreement with image simulations performed using different bonding

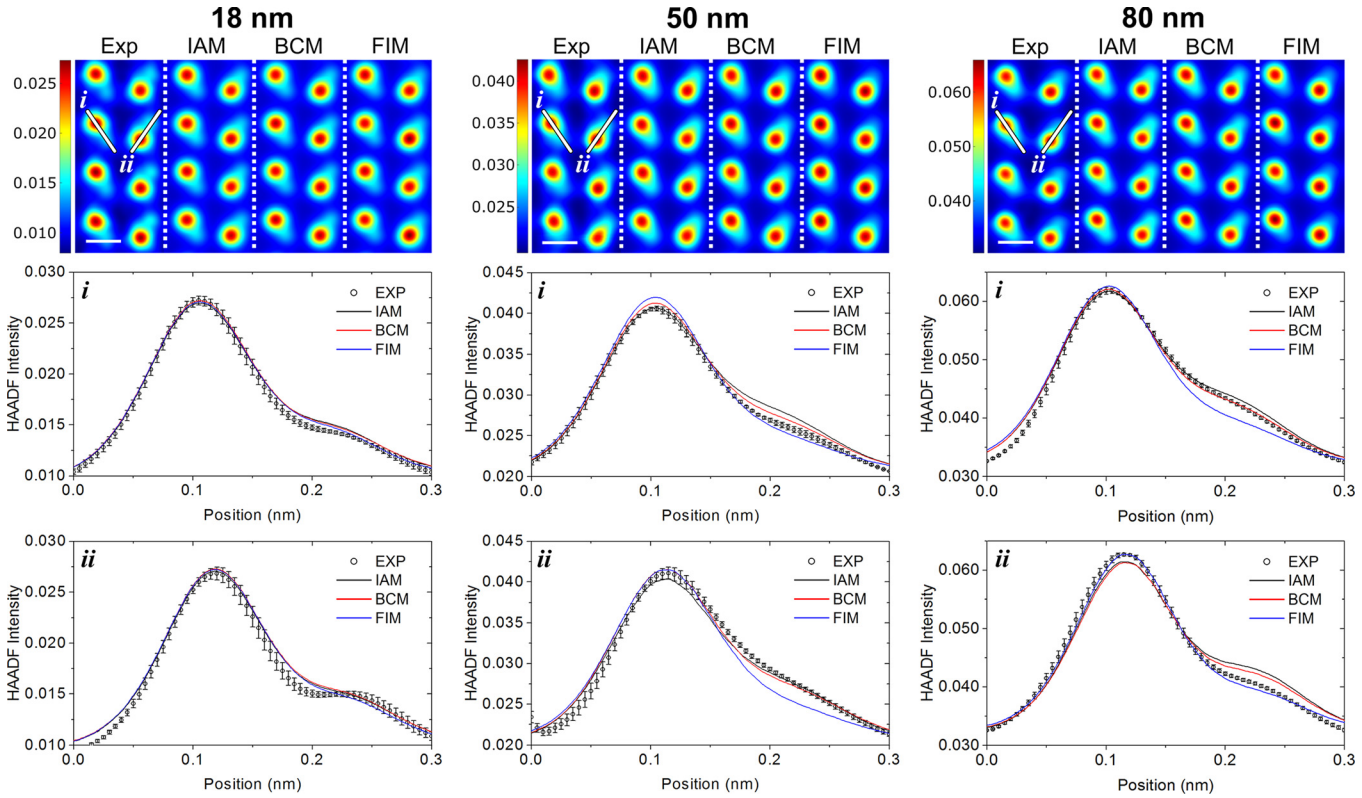

FIG. 6. (Color online) Comparison of experimental HAADF-STEM imaging of different sections of a $\langle\bar{2}110\rangle$-oriented AlN sample to corresponding simulations. Image regions are 2×1 rectangular unit cells in area, scale bar length is 2 Å. Simulated linescans for each bonding model were aligned to the experimental linescans by matching the peaks corresponding to Al columns. Error bars in experimental linescans correspond to one standard deviation of the linescan-to-linescan variation in the experimental image.

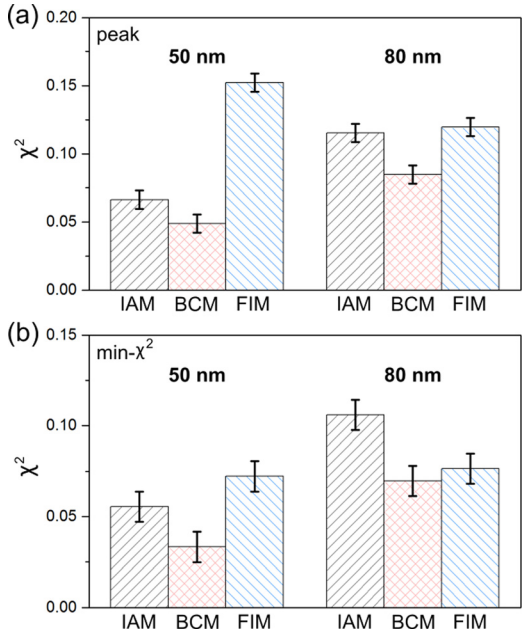

FIG. 7. (Color online) Sum-squared error of differences between experimental and simulation linescans. (a) Linescans for each bonding model were aligned to the experimental linescans by matching the peaks corresponding to Al columns. (b) Linescans for each bonding model were aligned to the experimental linescans to minimize sum-squared error. The uncertainties are estimated using the 18 nm thickness data as a reference case.

models. However, as can be seen from Fig. 7, in the AlN image data at thicknesses of 50 and 80 nm, exclusive best agreement between experiment and BCM simulation demonstrates the depth-dependent effect of chemical bonding on HAADF-STEM image contrast. Although the experimental images contain the effects of probe aberrations and effective source distribution, the differences between images simulated using each bonding model are preserved and a systematic best match exists. These differences confirm that the electron distribution in a polar crystal is best represented by covalent bonding in HAADF-STEM imaging, which differs significantly from an array of independent neutral atoms or an array of independent formal-charge ions.

IV. CONCLUSIONS

Quantitatively calibrated ADF-STEM images of polar light-element crystal AlN were conducted using a procedure that inverts the effect of detector nonuniformity from experimental data. Direct comparison to bonding-inclusive multislice simulations experimentally confirms the depth-dependent effect of bonding on ADF-STEM imaging, an effect explained and systematically examined in a companion computational study. This constitutes the first measurement of bonding effects in the widely used HAADF-STEM imaging mode, and encourages inclusion of bonding effects to improve the accuracy of TEM image simulation for crystals with highly polar bonding. Furthermore, it shows that while neutral-atom inputs can be measurably incorrect, fully ionic inputs are also problematic; proper bonding-inclusive inputs must reflect the true measure of interatomic charge transfer calculated from first principles.

Although the effects of chemical bonding on ADF-STEM imaging are measurable, they are subtle, requiring careful processing of experimental images and fine-tuning of simulation to discern them. Conventional IAM simulations are often adequate for qualitative agreement with experiment, and in many cases also for quantitative agreement. However, the intrinsic effect of net interatomic charge transfer on the channeling of a TEM beam in a crystal can only be addressed by bonding-inclusive simulation. Thus, use of bonding-inclusive simulation refines quantitative STEM imaging of polar single crystals. Studies of change transfer at defect sites in polar materials (e.g., dislocations, epitaxial interfaces[30]), where due to changes in composition of nearest neighbors and strain it will be enhanced, should benefit from such bonding-inclusive image simulation even more. The significance of bonding effects in light- versus heavy-element polar systems would be a natural progression from this study. The quantitative significance of including thermal vibration anisotropy and plasmon scattering in multislice simulations is also worthy of further consideration.

It should be noted that this study was limited by typical uncertainties in determining thickness, surface reconstruction and damage effects, effective source distribution, defocus, and astigmatism; reasonable final estimates of these quantities were made, but with limited confidence. This experience suggests that the development of automated, convenient routines for tasks such as accurate thickness measurement, detector calibration, source distribution determination, and residual astigmatism measurement are necessary prerequisites for widespread adoption of quantitative STEM methods.

ACKNOWLEDGMENTS

This work was supported by NSF MRSEC under Award No. DMR-1420013. J.T.H. received additional support from the University of Minnesota Graduate School Fellowship. STEM analysis was carried out in the Characterization Facility of the University of Minnesota, which receives partial support from the NSF through the MRSEC Program. Multislice simulations were performed using computational resources provided by the Minnesota Supercomputing Institute at the University of Minnesota. Matteo Cococcioni and Burak Himmetoglu provided DFT calculations.

[1]M. A. O'Keefe, P. R. Buseck, and S. Iijima, Nature **274**, 322 (1978).
[2]E. J. Kirkland, R. F. Loane, and J. Silcox, Ultramicroscopy **23**, 77 (1987).
[3]P. A. Stadelmann, Ultramicroscopy **21**, 131 (1987).
[4]M. L. Odlyzko, B. Himmetoglu, M. Cococcioni, and K. A. Mkhoyan, J. Vac. Sci. Technol. A **34**, 041602 (2016).
[5]J. Fertig and H. Rose, Optik **59**, 407 (1981).
[6]R. F. Loane, E. J. Kirkland, and J. Silcox, Acta Crystallogr., Sect. A **44**, 912 (1988).
[7]S. Hillyard, R. F. Loane, and J. Silcox, Ultramicroscopy **49**, 14 (1993).
[8]K. Ishizuka, J. Electron Microsc. **50**, 291 (2001).
[9]L. J. Allen, S. D. Findlay, M. P. Oxley, and C. J. Rossouw, Ultramicroscopy **96**, 47 (2003).
[10]C. Dwyer and J. Etheridge, Ultramicroscopy **96**, 343 (2003).
[11]M. Haider, S. Uhlemann, E. Schwan, H. Rose, B. Kabius, and K. Urban, Nature **392**, 768 (1998).
[12]P. E. Batson, N. Dellby, and O. L. Krivanek, Nature **418**, 617 (2002).
[13]P. D. Nellist *et al.*, Science **305**, 1741 (2004).

[14]R. Erni, M. D. Rossell, C. Kisielowski, and U. Dahmen, Phys. Rev. Lett. **102**, 096101 (2009).
[15]K. Kimoto, T. Asaka, T. Nagai, M. Saito, Y. Matsui, and K. Ishizuka, Nature **450**, 702 (2007).
[16]D. A. Muller, L. F. Kourkoutis, M. Murfitt, J. H. Song, H. Y. Hwang, J. Silcox, N. Dellby, and O. L. Krivanek, Science **319**, 1073 (2008).
[17]M. W. Chu, S. C. Liou, C. P. Chang, F. S. Choa, and C. H. Chen, Phys. Rev. Lett. **104**, 196101 (2010).
[18]K. Suenaga, T. Okazaki, E. Okunishi, and S. Matsumura, Nat. Photonics **6**, 545 (2012).
[19]L. J. Allen, S. D. Findlay, A. R. Lupini, M. P. Oxley, and S. J. Pennycook, Phys. Rev. Lett. **91**, 105503 (2003).
[20]J. M. LeBeau, S. D. Findlay, L. J. Allen, and S. Stemmer, Phys. Rev. Lett. **100**, 206101 (2008).
[21]J. M. LeBeau, A. J. D'Alfonso, S. D. Findlay, S. Stemmer, and L. J. Allen, Phys. Rev. B **80**, 174106 (2009).
[22]A. Rosenauer, K. Gries, K. Muller, A. Pretorius, M. Schowalter, A. Avramescu, K. Engl, and S. Lutgen, Ultramicroscopy **109**, 1171 (2009).
[23]J. M. LeBeau, S. D. Findlay, X. Wang, A. J. Jacobson, L. J. Allen, and S. Stemmer, Phys. Rev. B **79**, 214110 (2009).
[24]C. Dwyer, C. Maunders, C. L. Zheng, M. Weyland, P. C. Tiemeijer, and J. Etheridge, Appl. Phys. Lett. **100**, 191915 (2012).
[25]H. L. Xin, C. Dwyer, and D. A. Muller, Ultramicroscopy **139**, 38 (2014).
[26]R. Ishikawa, A. R. Lupini, S. D. Findlay, and S. J. Pennycook, Microsc. Microanal. **20**, 99 (2014).
[27]J. Hwang, J. Y. Zhang, A. J. D'Alfonso, L. J. Allen, and S. Stemmer, Phys. Rev. Lett. **111**, 266101 (2013).
[28]R. Ishikawa, A. R. Lupini, S. D. Findlay, T. Taniguchi, and S. J. Pennycook, Nano Lett. **14**, 1903 (2014).
[29]D. M. Smyth, Annu. Rev. Mater. Sci. **15**, 329 (1985).
[30]H. Y. Hwang, Y. Iwasa, M. Kawasaki, B. Keimer, N. Nagaosa, and Y. Tokura, Nat. Mater. **11**, 103 (2012).
[31]S. D. Findlay and J. M. LeBeau, Ultramicroscopy **124**, 52 (2013).
[32]G. T. Martinez, L. Jones, A. De Backer, A. Beche, J. Verbeeck, S. Van Aert, and P. D. Nellist, Ultramicroscopy **159**, 46 (2015).
[33]J. M. Lebeau, S. D. Findlay, L. J. Allen, and S. Stemmer, Ultramicroscopy **110**, 118 (2010).
[34]H. Schulz and K. H. Thiemann, Solid State Commun. **23**, 815 (1977).
[35]T. Yamazaki, M. Kawasaki, K. Watanabe, I. Hashimoto, and M. Shiojiri, Ultramicroscopy **92**, 181 (2002).
[36]S. E. Maccagnano-Zacher, K. A. Mkhoyan, E. J. Kirkland, and J. Silcox, Ultramicroscopy **108**, 718 (2008).
[37]J. Verbeeck, A. Beche, and W. Van den Broek, Ultramicroscopy **120**, 35 (2012).